Tectonophysics 682 (2016) 237–248

Contents lists available at ScienceDirect

Tectonophysics

journal homepage: www.elsevier.com/locate/tecto

Left-lateral shear inside the North Gulf of Evia Rift, Central Greece, evidenced by relocated earthquake sequences and moment tensor inversion

Athanassios Ganas *, Evangelos Mouzakiotis, Alexandra Moshou, Vassilios Karastathis

Institute of Geodynamics, National Observatory of Athens, 11810 Athens, Greece

ARTICLE INFO

Article history:
Received 17 July 2015
Received in revised form 14 May 2016
Accepted 19 May 2016
Available online 20 May 2016

Keywords:
Active tectonics
Earthquake
Stress inversion
Aftershock relocation
Shear
Evia, Central Greece

ABSTRACT

The use of local velocity model in the analysis of seismicity recorded by the Hellenic Unified Seismological Network (HUSN), provides the opportunity to determine accurate hypocentral solutions using the weighted P- and S-wave arrival times for the November 2013, November 2014 and June 2015 North Gulf of Evia (Euboea) sequences. The hypocentral locations, including the determination of the location uncertainties, are obtained applying the non-linear probabilistic analysis. We also calculated the moment tensor solutions for the main events as well as for the strongest aftershocks. The accurate determination of seismicity showed the activation of two left-lateral, NW-SE striking, near-vertical faults, one onshore near village Taxiarchis (2013 sequence) and one offshore (offshore Malessina Peninsula, 2015 sequence). The 2014 sequence, also offshore Malessina Peninsula ruptured an oblique-slip, north-dipping normal fault with a strike of N280–290°E. All three faults occur at depths 10–16 km, with rupture zone dimensions 5–6 km along strike and 3–4 km along dip. These aftershock depths indicate a seismogenic (brittle) zone of about 15 km in depth for this rift. The left-lateral kinematics indicates strain partitioning inside the rift because of E-W horizontal compression, also evidenced by GPS data. The moderate magnitude of earthquakes (M5.2 ± 0.1) indicates that strike-slip events have a minor contribution to the crustal deformation and to active tectonics of the Gulf.

1. Introduction

This work presents the results of the hypocentral relocation and stress inversion analysis for three recent earthquake sequences in the northern Gulf of Evia (Euboea), Central Greece (Fig. 1a; during 2013–2015). Gulf of Evia is a juvenile rift (Roberts and Jackson, 1991; Roberts and Ganas, 2000; Walker et al., 2010) with an overall strike of WNW-ESE, hosting a series of mostly north-dipping normal faults that are capable of rupturing up to M7 earthquake events (Ambraseys and Jackson, 1990). The existence of the rift at the western termination of the North Anatolian Fault (Hatzfeld et al., 1999) as well as the absence of M6+ events after 1894 (e.g. Ganas et al., 2006) provide this region with extra motives to study seismicity patterns. On 12 November 2013 (18:09, UTC) a moderate, $M_L = 4.8$ earthquake, occurred onshore northern Evia, near the village Taxiarchis (Fig. 1a; Moshou et al., 2015). For a period of one month 155 aftershocks were recorded with magnitude $M_L > 0.5$, while on the first day 85 earthquakes occurred; the largest of them with magnitude $M_L = 3.9$ (occurred on 13 November 2013 06:50 UTC). About one year later, on November 17, 2014, two shallow earthquakes with magnitude $M_L = 5.2$ occurred inside the northern Gulf of Evia (offshore), between Malessina Peninsula and Mountain Kandilli (Figs. 1a & 2; Table 1, event 1 & 2). Numerous aftershocks occurred up to January 2015, of which 454 events ($0.7 < M_L < 4.0$) were selected for further analysis. On June 9, 2015 a fourth, moderate $M_L = 5.2$ earthquake occurred south of the focal area of the 2014 main shocks (Table 1, event 3). The published focal plane solutions of the 2014 & 2015 events are shown in Table 1, mostly indicating normal faulting with a significant strike-slip component (event 1, event 2) or strike-slip faulting (event 3). The high quality of seismic data available in combination with a good knowledge of the local tectonics (e.g. Hatzfeld et al., 1999; Ganas and Papoulia, 2000; Sakellariou et al., 2007; Rondoyanni et al., 2007; Karastathis et al., 2007, 2011; Ganas et al., 2014a) prompted us to investigate these sequences in order to a) better locate the events and "image" the seismic faults and b) study the kinematics of the ruptures and tie them to the general strain field as was recently published by Kreemer et al. (2004), Müller et al. (2013), Chousianitis et al. (2013, 2015) and Vernant et al. (2014).

* Corresponding author.
E-mail address: aganas@gein.noa.gr (A. Ganas).

http://dx.doi.org/10.1016/j.tecto.2016.05.031
0040-1951/

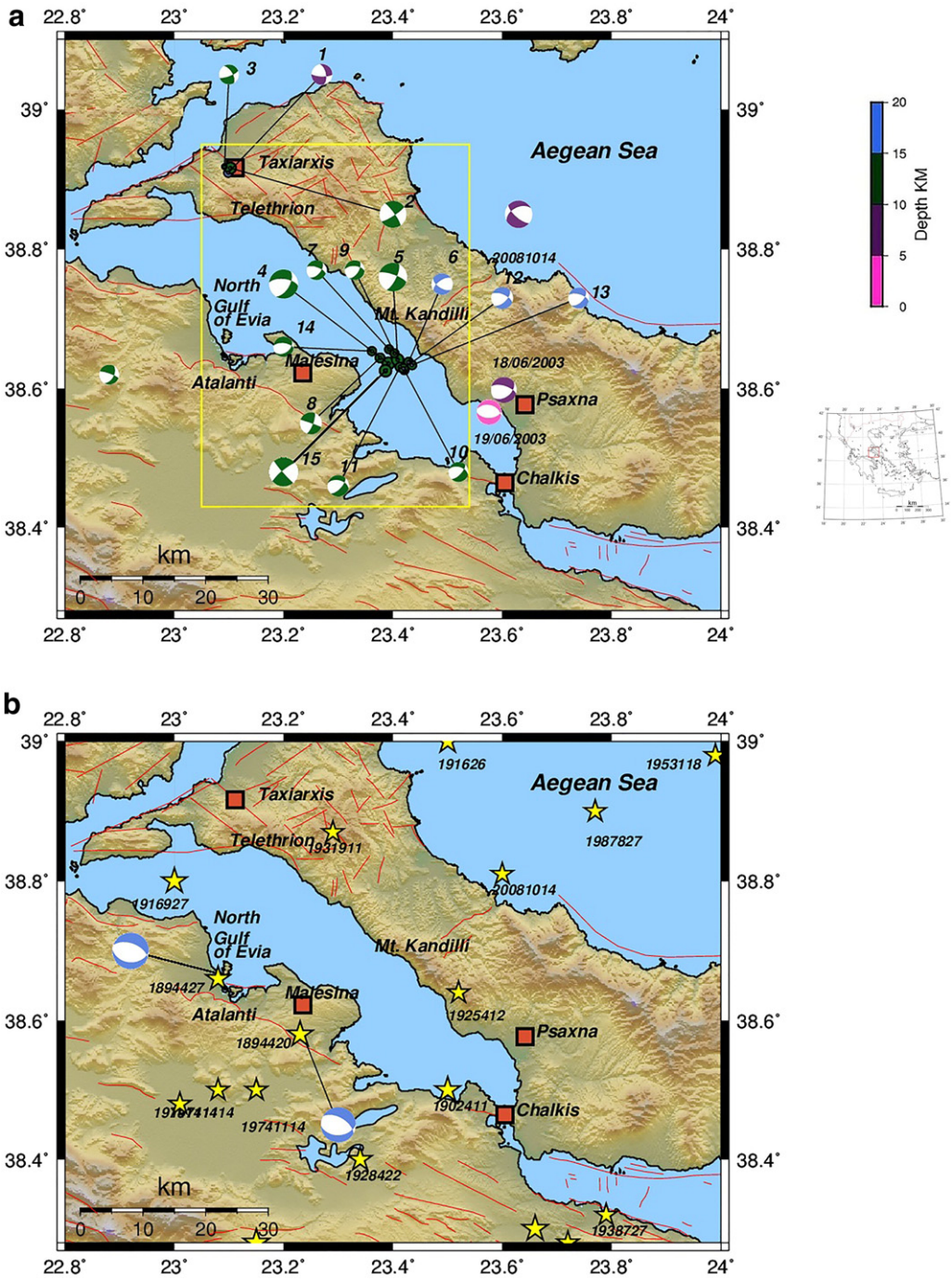

Fig. 1. a) Relief map of North Gulf of Evia region, Central Greece. Beach balls indicate focal plane solutions of recent, moderate seismic sequences (number above each event corresponds to number in Table 2). Red lines are active faults from Ganas et al. (2013). Yellow box shows extent of Fig. 2. Inset box lower right shows area inside Greece. B) Map showing post-1894 historical events (yellow stars) from Makropoulos et al. (2012) The 1894 focal mechanisms are from Ganas et al., (2006).

2. Tectonic setting

The North Gulf of Evia (Euboea; Fig. 1) is located between the transtensional North Aegean region (hosting branches of the north Anatolian fault system; Koukouvelas and Aydin, 2002; Kiratzi, 2002; Chatzipetros et al., 2013) and the rapidly extending Gulf of Corinth (Ambraseys and Jackson, 1990, 1997). Onshore syn-rift sequences are of Pliocene–Quaternary age (Mettos et al., 1991, 1992; Rondoyanni et al., 2007; Kranis, 2007). The most notable fault structure in the Gulf of Evia is the Atalanti fault zone (Fig. 1a) (Ganas et al., 1998; Pantosti et al., 2001; Pavlides et al., 2004) that consists of several segments of north-dipping active normal faults. Two major earthquakes that occurred in 20/04/1894 and 27/04/1894 with magnitudes of M = 6.4 and M = 6.6 respectively, have been associated to this fault system. However, no other M6+ events have been recorded in this rift since 1894 (Fig. 1b; see Ganas et al., 2006 for evolution of stress field). In the vicinity of the 2013–2015 sequences it is observed (Makropoulos et al., 2012; Fig. 1b): a M5.7 event in September 27, 1916; a M5.0 event in April 12, 1925 and a M5.0 event in September 9, 1931. Due to the 10+ km ambiguity in historical epicentral location we cannot associate those events with structures in the field. However, one submarine fault zone of E-W strike, the south-dipping Telethrion fault (Fig. 1a; equivalent to Edipsos segment in Ganas and Papoulia, 2000) can be considered as capable of hosting strong earthquakes (Sakellariou et al.,

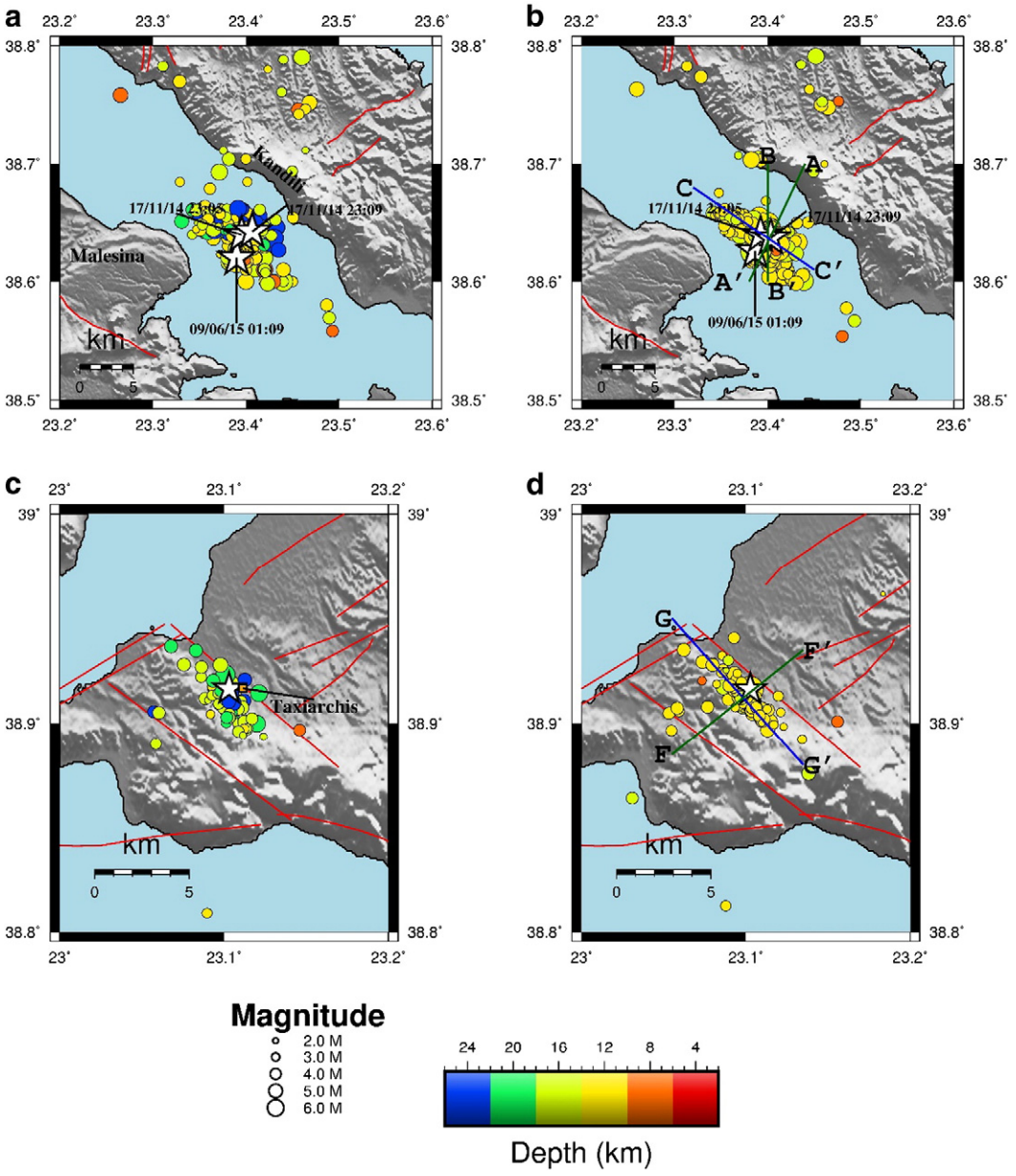

Fig. 2. Seismicity distribution with depth a) before b) after relocation for the Malesina –Kandili sequence (2014–2015), c) before and d) after relocation for the Taxiarchis (2013) sequence. Lines with capital letters show location of cross sections (AA', BB' and CC' in Fig. 8; GG' and FF' in Fig. 6). Red lines are active faults. White stars are epicenters of main events. Seismic stations used in relocation are shown in Fig. S1.

2007). Further south (up to Chalkis city; Fig. 1a) several E-W to NW-SE minor normal faults exist (Sakellariou et al., 2007; Karastathis et al., 2007) that are interpreted as secondary structures releasing Evia intra-block strain with moderate seismic potential (Ganas et al., 2014a). Since the beginning of instrumental recordings there have not been strike-slip earthquake sequences in the study area. Nevertheless, towards the north-east of the 2013 sequence (i.e. towards the shores of Aegean Sea) fault plane solutions of many earthquakes suggest predominant strike slip motions (Hatzfeld et al., 1999; Kiratzi, 2002). To the south-east of the 2014–2015 sequences a seismic swarm occurred during 2003 with mostly normal-slip kinematics (Psachna area, Fig.1a; Benetatos et al., 2004; Papoulia et al., 2006). The north Gulf of Evia is modeled as crustal block boundary by Vernant et al. (2014) across which there is an extension of 3.6 mm/yr and left-lateral shear of 2.5 mm/yr.

3. Methodology and data processing

3.1. Hypocentral relocation

The three seismic sequences with upper magnitudes $M_L = 4.9$ and $M_L = 5.3$, of 12 November 2013 17 November 2014 and June 9, 2015 respectively, have been relocated (Fig. 2) using broadband data from HUSN network (stations used are shown in supplementary Fig. S1). A 1-D velocity model on the basis of the 3-D local earthquake tomography model proposed by Karastathis et al. (2011; Fig. 3) was used, consisting of 6 layers of velocity model. The nodes are well distributed in seven horizontal layers (slices) at depths of 0, 1.5, 7, 12, 18.5 and 31 km, with the Moho depth at 31 km (Ganas et al., 2014a) (Table 3). For the 2013 seismic sequence the phase data from National Observatory of Athens include more than 12,700 P- and 4800 S-wave arrivals. Only

Table 1
Source parameters published by various institutions for the Nov. 17, 2014 event 23:06 UTC (event 1), Nov. 17, 2014 event 23:09 UTC (event 2), June 9, 2015 event 01:09 UTC (event 3). Mo is seismic moment, Mw is moment magnitude.

Institute	Lat (°)	Lon (°)	Mw	Mo (dyn*cm)	Depth (km)	Strike 1(°)	Dip 1(°)	Rake 1(°)	Strike 2(°)	Dip 2 (°)	Rake 2 (°)	Event
INGV	38.6500	23.4000	5.3	1.30E+24	18	43	55	−141	288	59	−42	1
USGS	38.6000	23.6700	5.4	1.54E+24	18	290	41	−31	45	70	−126	1
GFZ	38.6600	23.4000	5.2	8.80E+23	14	40	56	−140	286	58	−40	1
AUTH	38.6580	23.4112	5.2	6.34E+23	10	26	79	−161	292	71	−11	1
UOA	38.6433	23.4145	5.2	9.17E+23	13	275	58	−66	55	39	−123	1
NOA	38.6398	23.3953	5.2	8.50E+23	10	275	56	−67	57	40	−120	1
This study	38. 6360	23.3920	5.3	8.66E+23	14	280	60	−40	33	56	−143	1
INGV	38.6300	23.4300	5.2	7.50E+23	17	216	65	−168	121	79	−26	2
USGS	38.7000	23.2800	5.1	4.80E+23	18	126	60	−3	217	87	−150	2
GFZ	38.6300	23.3200	5.1	4.80E+23	14	305	89	−14	35	75	−178	2
NOA	38.6427	23.4067	5.1	5.93E+23	12	301	64	−39	50	55	−148	2
AUTH	38.6450	23.4310	5.0	3.95E+23	10	34	80	−166	302	76	−10	2
UOA	38.6437	23.3963	5.1	5.49E+23	12	294	67	−64	63	34	−136	2
This study	38.6413	23.4087	5.2	6.58E+23	13	290	75	−20	25	71	−164	2
INGV	38.6300	23.3400	5.3	1.3E+24	21	229	81	−177	139	87	−10	3
USGS	38.6700	23.3400	5.3	1.3E+24	14	227	81	−175	136	86	−9	3
GFZ	38.6200	23.3300	5.2	6.9E+23	10	139	88	9	48	81	178	3
AUTH	38.6400	23.4000	5.2	1.12E+24	10	51	81	−162	318	72	−9	3
NOA	38.6220	23.3890	5.2	7.81E+23	14	229	82	166	321	76	8	3
This study	38.6220	23.3890	5.2	6.58E+23	11	230	80	−175	139	85	−10	3

events with at least 8 P-wave and 4 S-wave arrivals having an azimuthal gap lower than 180°, location RMS lower than 0.8 s (Figs. 4, 5) and vertical and horizontal errors lower than 1.5 km were selected for processing. The non-linear location method of NonLinLoc (Lomax et al., 2000) was used. NonLinLoc gives, a complete probabilistic solution expressed in terms of a posterior density function (PDF) (Tarantola and Valette, 1982). The software incorporates a 3D version of the Eikonal finite-difference scheme (Le Meur, 1994; Le Meur et al., 1997) for the calculation of travel-times between a station and all nodes of a 3D velocity grid. This results in the creation of a travel time grid for each station in the study area. Those grids are retrieved in a later step, in order to calculate the optimal hypocenter location using the Oct-tree importance sampling algorithm (Lomax and Curtis, 2001) which uses recursive subdivisions and sampling of cells in order to converge to the optimal hypocentral location. Throughout the above-described procedure, the PDF is calculated using the equal-differential-time (EDT) likelihood function (Font et al., 2004). Contrary to the typical least-squares approaches, the difference between observed and synthetic travel times is calculated for pairs of stations and the sum is taken over all possible pairs. This results in a number of advantages. For datasets where mispicked observations (or outliers) have to be taken into account, the EDT likelihood function is more accurate, providing a more reliable uncertainty estimate. Moreover, it is independent of the origin time, thus the 4-D problem of hypocenter location reduces to a 3-D search over spatial location of the hypocenter. As a result, the algorithm was able to detect mispicked phases in our dataset and downweight them significantly, thus improving the location solution (horizontal location error is between 400 m and 1.2 km; Figs. 4, 5). On the contrary, in the initial location analysis by NOA, such outliers affected the final solutions. Moreover, the non-linear location method of NonLinLoc is not affected by the shortcomings of linearized location methods, particularly the dependence of the solution on the quality of the initial guess and the instability for poorly constrained earthquake locations (Husen and Hardebeck, 2010). Events locations acquired at local minima with the initial location analysis were now better resolved with the use of this non-linear location method.

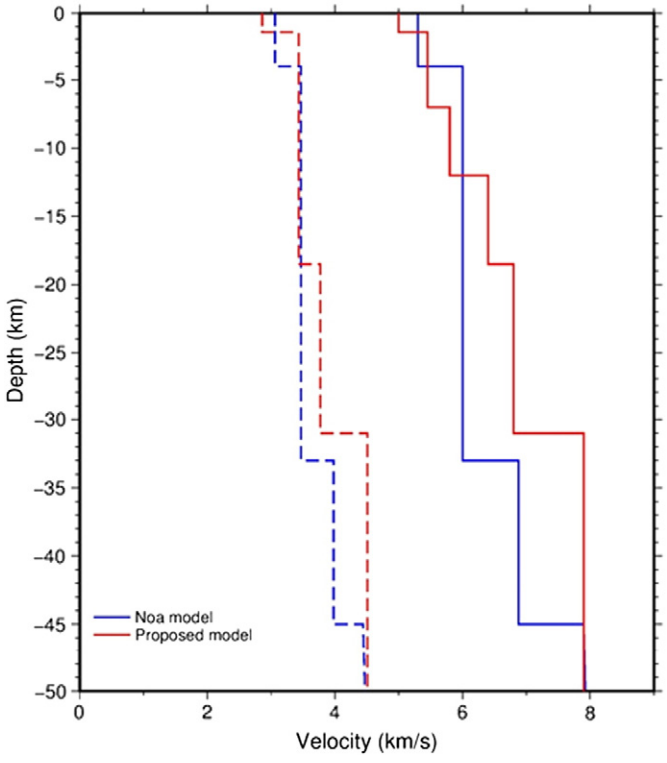

Fig. 3. The P-wave (red continuous line) and S-wave (red dashed line) velocity models proposed for the Central Greece based on the earthquake tomography results of Karastathis et al. (2011) and used for the relocation of the 2013 Kalidromon seismic sequence (Ganas et al., 2014a). The P and S-wave velocity models, used for the daily seismicity monitoring by NOA are also shown with blue continuous and dashed lines respectively.

The relocation of the November 2013 Taxiarchis sequence (Fig. 2c,d) revealed the activation of a NNW-SSE fault, with near-vertical dip (Fig. 6a) at mid-crustal depths (11–14 km). The "imaged" fault plane has dimensions 5 km along strike with 3–4 km along-dip (Fig. 6b), while the focal mechanism was determined at this study by moment tensor inversion (see Section 3.2 for method) as left-lateral strike-slip (Table 2; nodal plane 1; strike/dip/rake 325°/80°/−10°).

The relocated aftershock activity of the two November 2014 events clearly reveals a WNW-ESE striking fault about 5 km offshore Malessina Peninsula (Fig. 2a, b and Fig. 7) that extends from 10 km up to a depth of 16 km (see cross-sections in Fig. 8a, b). On the other hand, the 2015 aftershock hypocenters are well clustered and indicate the activation of a left-lateral, near-vertical fault, striking NW-SE, and located 2 km towards the south of the 2014 sequence (Figs. 7 & 9; orientations of the

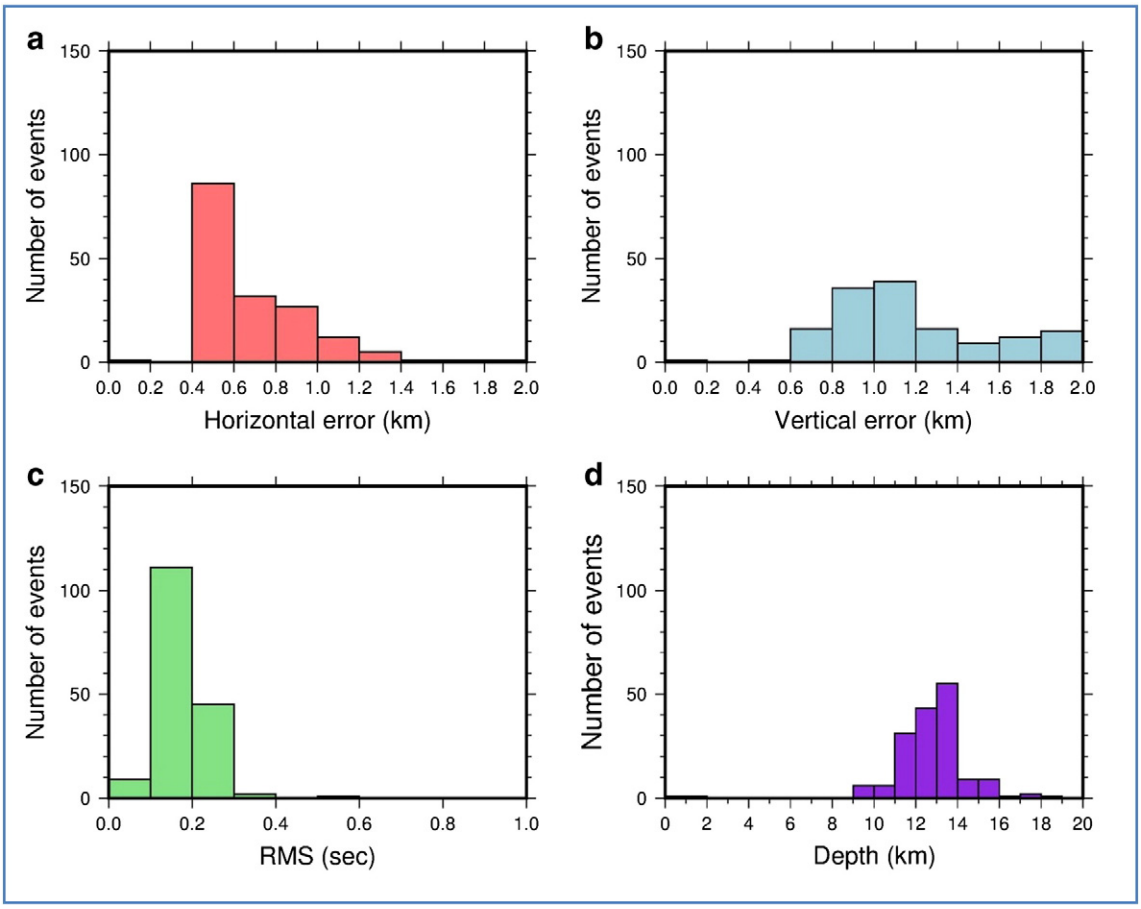

Fig. 4. Histograms depicting descriptive statistics for Taxiarchis sequence (2013; N = 267) a) horizontal error of location b) vertical error of locations c) root-mean-square error of the solution and d) depth distribution of events. See Fig. 2d for location of events.

seismicity trends differ). A cross-section in Fig. 8b shows that the 2015 activated fault dips steeply to the North. We interpret these features as two distinct faults because a) in seismicity cross sections the 2014–2015 foci clusters plot separately (Fig. 8 see foci with different colors; blue depicts 2015 events) b) the distance between the two clusters is much greater than the maximum lateral location error (1.2 km; Fig. 5) and the majority of 67% confidence ellipsoids do not overlap (Fig. 9) c) the focal mechanisms of the mainshocks (Nov. 17 2014 vs June 9 2015) are different (see next section), consistent with the interpretation that two distinct structures ruptured. This distinct image of the 2014 vs. 2015 seismicity highlights the resolving power of the relocation procedure used. However, this consideration is valid only under the assumption that there is not any abrupt lateral anomaly in the local velocity structure.

3.2. Moment tensors

The second part of this study is the determination of the focal mechanisms and the calculation of the source parameters (strike, dip, rake, depth and moment magnitude) for the larger events. Seismological broadband data from HUSN were collected and analyzed in order to determine the source parameters of the moderate events. For this purpose, we selected and analyzed the data of 10 broadband seismological stations with three components (see Fig. S2 for location of stations). A linear, time-domain moment tensor inversion method with a point source approximation is applied to the three component waveforms of each event. The method uses the long period part of the signal to invert for the deviatoric part of the moment tensor and is fully described in a number of publications, most notably Randal (1994), Ghose et al. (1998), and Stich et al. (2003). We included in the inversion at least three stations that covered different azimuths on the focal sphere and with an epicentral distance not exceeding 250 km. Five stations at epicentral distances less than 250 km were used for the 12/11/2013 (18:09:27, UTC) event, six and seven stations at epicentral distances less than 230 km were used for the two events on 17/11/2014 (23:05:55 and 23:09:03, UTC) respectively and finally seven stations at epicentral distances less than 240 km for the 09/06/2015 (01:09:03, UTC) event. We calculated Green's functions for different depths using the reflectivity method of Kennett (1983) as implemented by Randal (1994), using the epicenter location provided by the manual analysis and assuming a delta source time function for small events. For moderate to large events the Green's functions were convolved with a trapezoid of appropriate length prior to the inversion. Data preparation included the reduction of waveforms to displacement and rotation of horizontal components to radial and transverse with respect to the event's epicenter.

Moment tensor inversions are usually performed in the frequency band 0.05–0.02 Hz for small earthquakes and in the band 0.05–0.01 Hz for large events. The limited bandwidth of our instruments means that inversions should be performed in a relatively narrow range of frequencies with 0.05 Hz being the lower cutoff frequency. Both the observed waveforms and Green's functions were filtered between 0.05 and 0.08 Hz using a two-pole Butterworth filter and aligned according

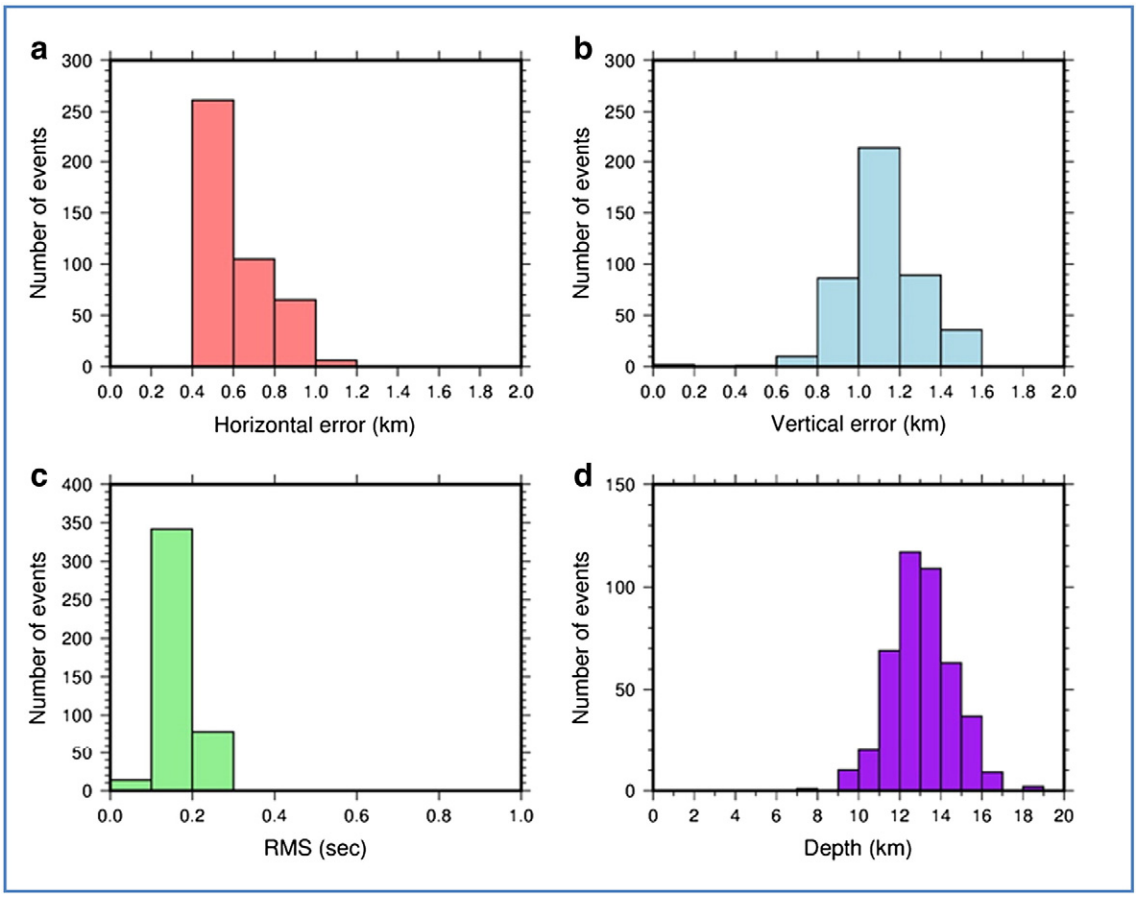

Fig. 5. Histograms depicting descriptive statistics for Malesina–Kandilli sequence (2014 and 2015; N = 454) a) horizontal error of location b) vertical error of locations c) root-mean-square error of the solution and d) depth distribution of events. See Fig. 2b for location of events.

to their arrival times in order to minimize the effects of the assumed velocity structure and any source mislocation. Test inversions showed that inverting waveforms longer than 60 s resulted in much higher misfits, since our simple velocity models cannot predict complicated waveforms at the 0.05–0.08 Hz frequency band in which we are working. Therefore in all our inversions we use a fixed wave form length of

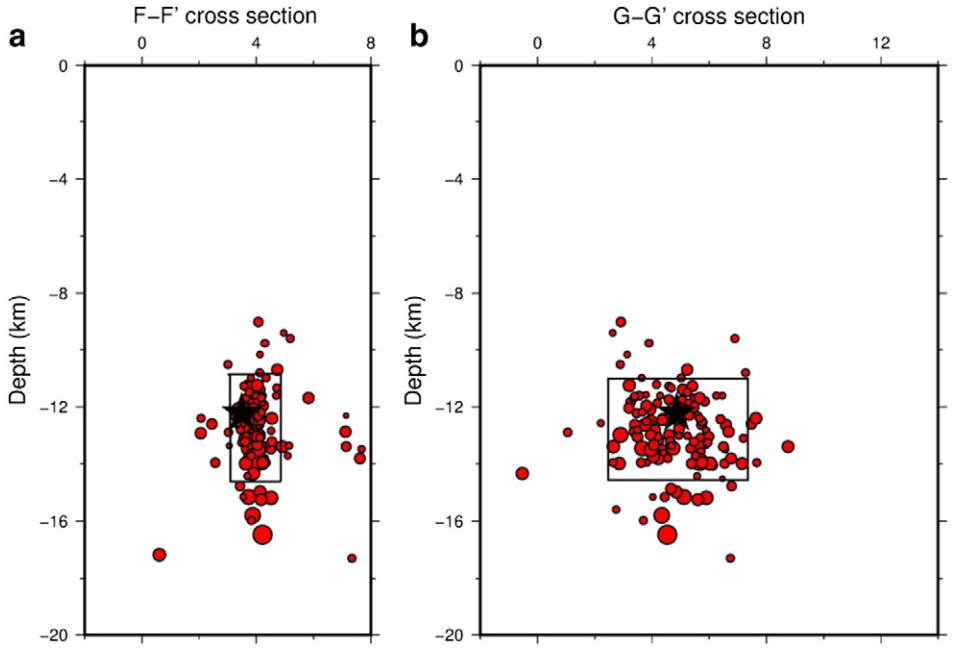

Fig. 6. Cross-sections of Taxiarchis sequence (see Fig. 2d for map view): a) across strike (F-F′) b) along strike (G-G′). Rectangles depict dimensions of activated fault. Black star indicates relocated hypocenter of mainshock (M = 4.9). The depth of 12 km agrees within the margin of error with the centroid depth (11 km; see Table 2).

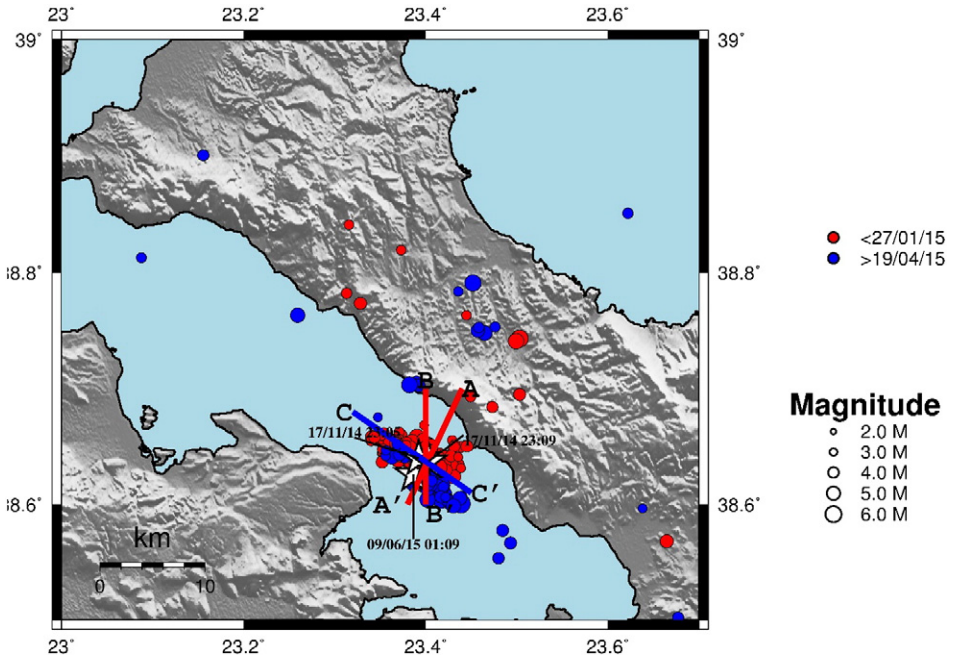

Fig. 7. Map of relocated events (solid circles) of the 2014–2015 Malesina–Kandilli sequence. Red circles depict events before Jan. 27, 2015. Blue circles depict events after 19 April 2015.

70 s, which is three times the maximum period of our observations (20 s). Initial inversions were performed at a coarse depth interval of 5 km followed by a finer one every 1–2 km around the depth that exhibited the lowest misfit (for intermediate-depth events these values become 10 and 5 km, respectively). The quality of the results of moment tensor solutions can be evaluated by considering the average misfit and the compensated linear vector dipole (CLVD; Konstantinou et al., 2010). The source parameters of fifteen (15) earthquakes with magnitudes 3.5 < Mw < 5.2 are shown in Table 2 while full documentation for each event is given in supplementary Fig. S3.

For the 2013 Taxiarchis source mechanism determination revealed strike-slip faulting with the best fit solution of strike = 325°, dip = 80°, rake = −10°, moment magnitude 4.9 and focal depth at 11 km (Table 2; Fig. S3a). The seismic moment is determined Mo = $2.48 \cdot 10^{23}$ dyn·cm, the calculated double couple (DC) was found equal to 90%. The source parameters of the two 2014, shallow events with similar magnitudes Mw = 5.3 and 5.2, on 17 November 2014 (23:05 and 23:09, UTC) were calculated using the moment tensor inversion method, as well. Both of the two events, normal-oblique slip type faulting was revealed after applying the inversion. The obtained focal mechanism for the first earthquake is strike = 280°, dip = 60° and rake = −40° (Supplementary Fig. S3b). The seismic moment is equal to Mo = $8.66 \cdot 10^{23}$ dyn·cm, for a focal depth equal to 14 km while for the second is strike = 290°, dip = 75° and rake = −20° (Fig. S3c). The inversion resulted in a DC (Double-couple) value equal to 93%. The seismic moment calculated was Mo = $6.58 \cdot 10^{23}$ dyn·cm and the depth at 13 km. The 2015 event source parameters (Mw = 5.2) are strike = 139°, dip = 85° and rake = −10° (Supplementary Fig. S3d). We also performed sensitivity tests to examine if the formal errors are representative of the actual resolving power of the network and inversion method used, focusing on the influence of the crustal velocity model (supplementary Figs. S4, S5 and S6). A summary of the quality parameters of each solution such as misfit and CLVD shows values between 0.12–0.22 (for misfit) and 5.2–9 (for CLVD). The obtained results confirm the robustness of our method.

Furthermore, the focal mechanisms (Figs. 1a; S3a,b,c, and d) of 12 November 2013, 17 November 2014, and 9 June 2015 events indicate either NE-SW right lateral strike-slip or NW-SE left lateral strike-slip motion. Because the aftershock hypocenters are aligned along the NW-SE orientation (Fig. 2), we interpret these events as left lateral strike-slip.

3.3. Stress inversion

We obtained the orientation of the local stress-field using the iterative stress inversion of Vavryčuk (2014) that is based on Michael's (1984) method. It is well known that stress inversions from focal mechanisms require knowledge of which nodal plane is the fault. If such information is missing, and faults and auxiliary nodal planes are interchanged, the stress inversions can produce inaccurate results. Vavryčuk (2014) showed that the linear inversion method developed by Michael is reasonably accurate when retrieving the principal stress directions even when the selection of fault planes in focal mechanisms is incorrect. He modified Michael's method and inverted jointly for stress and for fault orientations. The fault orientations are determined by applying the fault instability constraint and the stress is calculated in iterations. The input data comprise the Malesina–Kandilli events, namely 4–15 of Table 2 (i.e. 12 focal mechanisms for the period 2014–2015). As from relocation (Fig. 2) we already determined a general NW-SE alignment of seismicity we entered into the stress inversion code the nodal planes with NW-SE (±30°) strike. In addition, we estimate an error of 10° in strike and 5° in the dip-angle in our data. We found that the tectonic stress is characterized by the horizontal σ_3 axis, while the σ_2 and σ_1 axes significantly deviate from both the horizontal and vertical directions, respectively (Fig. 10a). The retrieved maximum compression (tectonic stress σ_1) is 26° from vertical (Fig. 10a). The obtained stress axes are (see Table 4) σ_1 (64°/267° plunge/azimuth), σ_2 (25°/76°) and σ_3 (4°/168°), respectively. The P/T axes with retrieved principal stress directions and the confidence limits of the principal stress directions retrieved by the iterative method are shown in Fig. 10, where a high confidence is calculated for the horizontal axis (σ_3; Fig. 10b; red, green and blue colors correspond to the σ_1, σ_2 and σ_3 stress directions, respectively). Regarding the azimuth errors in our stress model we assume an error of 6–7° in the obtained stress directions as in Vavryčuk (2014). We note that a misfit (or deviation) between observed and predicted slip direction of 6° was obtained from stress inversion analysis of the Skyros 2001 earthquake focal mechanisms (Ganas et al., 2005), that is for an earthquake with similar

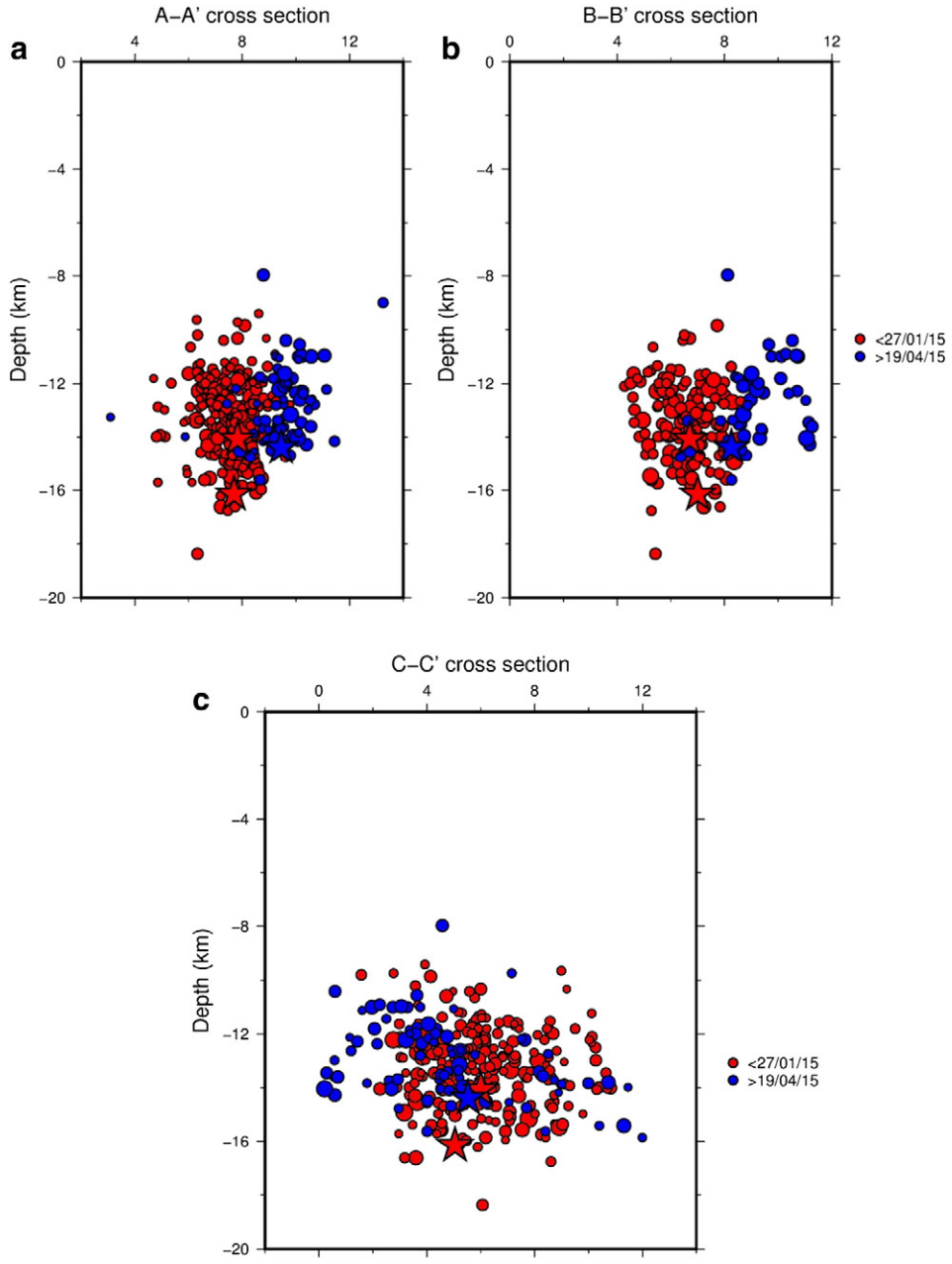

Fig. 8. Cross-sections of Malesina–Kandilli sequence (see Fig. 7 for map view): a) across strike A-A´ b) across strike B-B´ (along the N-S direction). Red circles represent event of the 2014 sequence, blue circles of the 2015 sequence, respectively. Stars indicate hypocentre of mainshocks. It is evident the formation of two clusters of foci. The 2015 sequence dips to the north. Cross-sections of offshore Malesina sequence: c) along strike.

kinematics (left-lateral strike-slip) that occurred 90 km to the east of the 2014–2015 events.

The N12°W (±7°) orientation of the least principal tectonic stress differs by an amount of 32° (±7°) with the geodetic data published by Chousianitis et al. (N20°E; 2013–2015; see orientation of principal horizontal strain rate axes in Fig. 11; also subjected to 5° azimuthal error), as well as by an amount of 27 (±7°) degrees with the fault-slip data of Roberts and Ganas (2000; N14–15°E). This result may be a true difference in the extension axis due to the different deformation patterns between the upper crust (reflected in both geodetic and geological data) and the middle crust (reflected in our seismic data). However, we refrain from drawing a solid conclusion on this due to the relatively small size of our focal mechanism sample (N = 12).

4. Discussion

Our high-resolution aftershock relocation and moment tensor analysis of the 2013–2015 Gulf of Evia seismic sequences showed the activation of three (3) "blind" faults with a significant left-lateral slip component. The first fault is located near the village Taxiarchis, onshore North Evia (Figs. 1a and 2d). Two seismic faults are located offshore Malesina–Kandilli (Figs. 2b; 9) not ignoring that during activation of aftershock sequences many aftershocks are off-fault aftershocks. The relocated aftershock hypocenters (Fig. 2) are aligned along the NW-SE orientation (Figs. 9 & S3), so we interpret these events as left lateral strike-slip. This is the first time that left-lateral shear is unequivocally documented by seismic data inside the north Gulf of Evia as previous

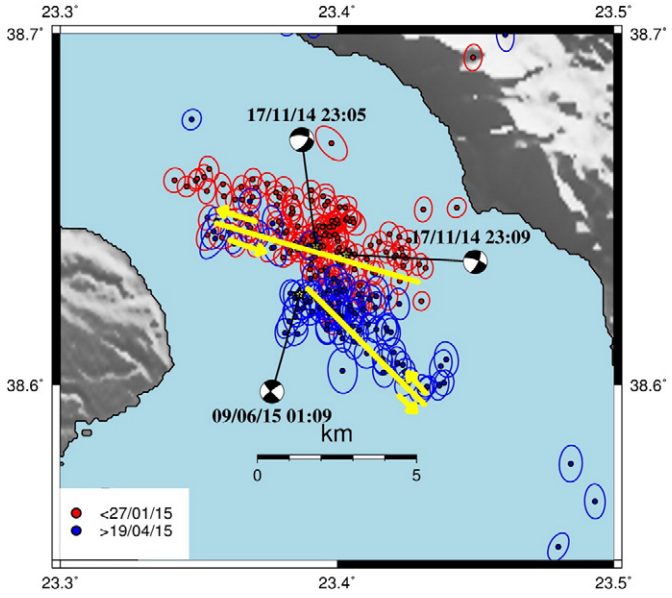

Fig. 9. Map of relocated aftershocks (solid circles) of the 2014–2015 Malesina–Kandilli sequence with 67% confidence ellipses of event location. Red circles depict events before Jan. 27, 2015. Blue circles depict events after 19 April 2015. Stars indicate mainshock locations. Beachballs show moment tensor solutions for the three earthquakes, plotted using a lower-hemisphere stereographic projection. Thick yellow lines depict locations of seismic faults with arrows indicating relative sense of motion across the fault.

focal plane solutions included isolated events only (e.g. Hatzfeld et al., 1999; Kiratzi, 2002) because of the lack of a) sufficient number and b) good-quality aftershock data. Previously, the limit for left-lateral tectonics was considered the eastern coastline of mainland Greece (Evia, Thessaly), on the basis of geodetic data (Kreemer et al., 2004; Müller et al., 2013).

Left-lateral shear can be part of the active tectonics in this young rift for the following reasons: a) the activated faults are compatible to the regional stress field because the T-axis azimuth of the local stress field (N168°E; Fig. 10) is close to the general N180°E crustal extension, demonstrated by geological (Roberts and Ganas, 2000; Rondoyanni et al., 2007) and geodetic data (Davies et al., 1997; Müller et al., 2013; Chousianitis et al., 2013, 2015) and b) the strike of the activated faults (N280°–325°E) also fits to the present-day strain field in terms of fault kinematics. In this part of Central Greece the general N-S extension rate of about 60–80 ns/yr (Chousianitis et al., 2015; 1 nstrain corresponds to 1 mm shortening or lengthening over a distance of 1000 km) is accompanied by E-W compression of −20 to −30 ns/yr (Kreemer et al., 2004; Chousianitis et al., 2013; Fig. 11). In particular, the baseline between stations 061A and 026A (Fig. 11) is shortened at 2 mm/yr (Chousianitis et al., 2013) equivalent to −27 ns/yr, way above the error estimates of the method (5–10 ns/yr). On the contrary, extensional strains are evident between stations 061A and 024A (+53 ns/yr; east end of the rift), as well as between stations 072A and 015A (+119 ns/yr; west end of the rift). The horizontal compression is due to the westward movement of the Anatolia microplate and is the dominant mode of deformation in the central Aegean Sea (see for example the 2001 left-lateral Skyros event; Benetatos et al., 2002, Ganas et al., 2005; the 2013 right-lateral Lemnos event, Ganas et al., 2014b). Therefore, we interpret the occurrence of moderate sequences ($4 < M < 5.5$) with horizontal-slip kinematics inside the Gulf of Evia rift as a response of the elastic crust to this compression. These relatively small faults (dimensions 5–6 × 3–4 km; length, width), thus, serve as to release strain accumulated along their surfaces because they are compatibly oriented structures to accommodate the strike-slip component of active tectonics. Moreover, in the same region there are several conjugate structures to the 2013/2015 sequences such as NE-SW oriented, right-lateral and oblique-slip faults that also accommodate present-day strain. Examples of the latter structures include the 14 October 2008 Mantoudi earthquake sequence (offshore NE Evia island; Fig. 1; Roumelioti and Kiratzi, 2010) and the transverse fault zones onshore Evia island that show Quaternary activity (Fig. 1; Palyvos et al., 2006).

In addition, we see no big differences in the depth-range of seismic faulting between the east end of this rift and the more centrally-located, Kallidromon 2013 sequence (west of station ATAL in Fig. 11; Ganas et al., 2014a), i.e. seismicity occurs in the depth range 10–16 km vs 8–13 km in Kallidromon. These aftershock depths indicate a seismogenic (brittle) zone of about 15 km in depth for this rift. In terms of magnitude, this seems to be characteristic of immature faults regarding their seismic potential, however, these earthquakes do present challenges in interpreting their initiation regarding their location: are these "blind" faults randomly located or they are related to viscous shear zones further below? Moreover, it seems that the strike-slip kinematics at mid-crustal depths may explain the deviation of σ_1 (principal stress) axis plunge from vertical with depth (26° from vertical; Table 4). In turn, this is probably related to the difference in σ_3 azimuth between the local stress and the field data from geology (Roberts and Ganas, 2000) and geodesy (Müller et al., 2013; Chousianitis et al., 2015). We need more data on the stress field at those depths to statistically document or not a rotation of σ_3 (the least principal axis) inside the rift.

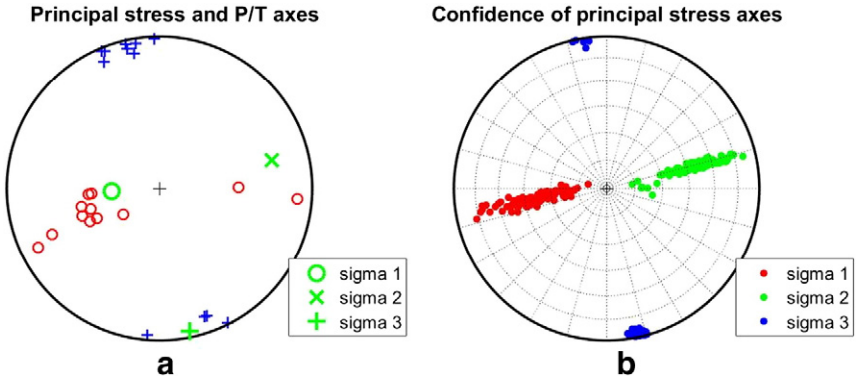

Fig. 10. Iterative inversion for stress using the twelve (12) focal mechanisms in the offshore Malesina–Kandilli region of the North Gulf of Evia rift. a) P/T axes with retrieved principal stress directions, P = red circles, T = blue crosses, b) confidence limits of the principal stress directions.

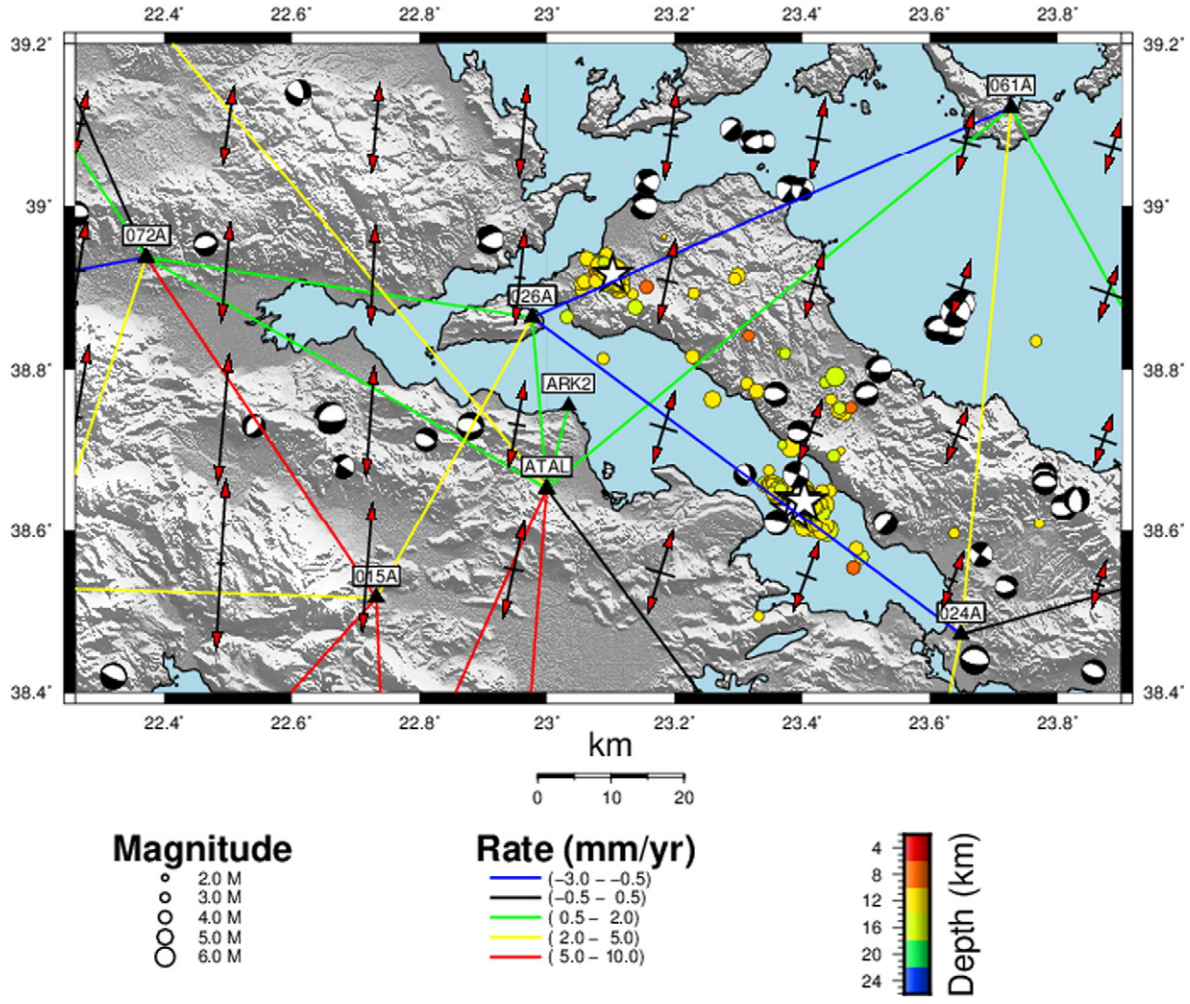

Fig. 11. Map of relocated events (solid circles) of the 2013–2015 Gulf of Evia sequences together with baselines of continuous GPS stations, calculated by Chousianitis et al. (2013). Baseline color is proportional to change rate of line length (in mm/yr). Principal strain rate axes for the region are also shown after Chousianitis et al. (2015) with red arrowhead indicating azimuth of extension, blue indicating shortening, respectively. Beachballs represent focal mechanisms from the on-line NOA catalog (period 2005–2013). White stars are mainshocks.

5. Conclusions

a) The accurate determination of 2013 seismicity (267 events) onshore North Evia (Euboea) shows the activation of a strike slip fault (preferred nodal plane of 325°/80°/−10°; Taxiarchis sequence; Fig. 1a) at depths 11–14 km.

b) The 2014 and 2015 relocated events (N = 454) allowed us to identify two active faults in this offshore area of the north Gulf of Evia, at depths 10–16 km, by locating linear patterns of aftershocks (Figs. 7, 8 9) and to analyze the stress field using stress inversion on the activated fault planes (Fig. 10). The 2014 sequence ruptured a N280°–290°E striking, 60°–75° dipping, oblique-slip fault. A near-

Table 2
Focal mechanisms of the main events of Gulf of Evia sequences as determined in this study. Mo is seismic moment, Plane 1 is first nodal plane, Plane 2 is second nodal plane, CLVD is compensated-linear-vector-dipole. Moment tensor solutions of this study are shown in Supplementary Fig. S3.

N_r	Origin		Location		M_o (dyn*cm)	M_w	Depth		Plane 1			Plane 2			CLVD (%)	No. of stations
	Date	Time	Lat (°)	Lon (°)			Catalog	MT	Strike°	Dip°	Rake°	Strike°	Dip°	Rake°		
1	131104	22:09:17.4	38.9095	23.0988	0.479E+22	3.80	16.4	9	350	57	−20	91	73	−145	11	4
2	131112	18:09:27.8	38.9162	23.1027	0.248E+24	4.90	12.2	11	325	80	−10	57	80	−170	10	5
3	131113	06:50:24.8	38.9183	23.0918	0.289E+22	3.60	13.9	13	330	60	−17	69	75	−149	7	4
4	171114	23:05:55.8	38.6360	23.3920	0.866E+24	5.30	14.8	14	280	60	−40	33	56	−143	9	6
5	171114	23:09:03.5	38.6413	23.4087	0.658E+24	5.20	13.8	13	290	75	−20	25	71	−164	5.2	7
6	171114	23:13:29.3	38.6380	23.4287	0.748E+22	3.90	10.6	15	123	58	−36	234	60	−142	6	4
7	171114	23:18:46.9	38.6563	23.3930	0.289E+22	3.60	12.5	12	290	65	−40	43	50	−147	8	5
8	171114	23:40:36.6	38.6440	23.3765	0.127E+23	4.00	12.4	12	290	88	−16	23	74	−170	9	5
9	181114	00:18:27.3	38.6505	23.4030	0.289E+22	3.60	11.4	11	275	55	−42	32	57	−137	7	5
10	181114	00:53:59.7	38.6263	23.4210	0.289E+22	3.60	13.4	14	287	46	−35	43	66	−130	6	4
11	181114	01:13:47.3	38.6310	23.4127	0.748E+22	3.90	11.3	12	285	45	−37	43	65	−129	8	4
12	191114	00:37:26.8	38.6290	23.4195	0.127E+23	4.00	12.5	16	294	62	−39	45	56	−145	6	4
13	191114	19:54:08.6	38.6337	23.4350	0.519E+22	3.80	11.2	15	43	54	−141	288	59	−43	7	4
14	201114	16:26:22.5	38.6537	23.3617	0.433E+22	3.70	14.8	14	277	59	−65	57	39	−125	7	4
15	090615	01:09:03:0	38.6220	23.3890	0.658E+24	5.20	13.0	11	230	80	−175	139	85	−10	8	7

Table 3
The layers of the velocity model that were used in this study (after Ganas et al., 2014a). The ratio Vp/Vs was set at 1.73. The crust–mantle boundary is assumed at 31 km depth.

Depth (km)	V_p (km/s)
0.0	5.0
1.5	5.45
7.0	5.8
12.0	6.4
18.5	6.8
31.0	7.9

Table 4
Parameters of the local (Malesina–Kandilli) stress field determined from iterative stress inversion analysis (Vavryčuk, 2014). N = 12 focal mechanisms with M > 3.8.

Stress axis	Azimuth (degrees)	Plunge (degrees)
Sigma 1	267	64
Sigma 2	76	25
Sigma 3	168	4

vertical, strike-slip fault (139°/85°/−10°) was activated during the 2015 offshore sequence.

c) The focal mechanisms (Fig. S3) of 12 November 2013, 17 November 2014, and 9 June 2015 events indicate either NE-SW right lateral strike-slip or NW-SE left lateral strike-slip motion. Because the aftershock hypocenters are aligned along the NW-SE orientation (Fig. 2), we interpret these events as left lateral strike-slip. This is the first time that left-lateral shear is clearly documented inside the Gulf of Evia rift.

d) These aftershock depths indicate a seismogenic (brittle) zone of about 15 km in depth for the Gulf of Evia rift.

e) The strike-slip faults are activated because of an E-W component of shortening strain (Fig. 11) and they accommodate a moderate contribution to the crustal deformation and to active tectonics of the Gulf of Evia.

Acknowledgments

We thank three anonymous reviewers for their useful comments and the Editor Rob Govers for his editorial assistance. We thank Zafeiria Roumelioti and Ioannis Kassaras for discussions. We acknowledge the use of HUSN (Hellenic Unified Seismograph Network) data. We would like to thank the NOA scientific personnel for phase picking. The open-source software GMT http://www.soest.hawaii.edu/gmt/ was used to make several figures. This research was funded by GSRT (Greek Secretariat for Research and Technology) under the Act "Infrastructure Upgrade for Seismic Protection of the Country and Strengthen Service Excellence through Action – "SHIELD – ASPIDA"" implemented under the Action "Development proposals for Research Bodies – KRIPIS".

Appendix A. Supplementary data

Supplementary data to this article can be found online at http://dx.doi.org/10.1016/j.tecto.2016.05.031.

References

Ambraseys, N.N., Jackson, J.A., 1990. Seismicity and associated strain of Central Greece between 1890 and 1988. Geophys. J. Int. 101, 663–708.
Ambraseys, N.N., Jackson, J.A., 1997. Seismicity and strain in the Gulf of Corinth (Greece) since 1694. J. Earthq. 1, 433–474.
Benetatos, C., Roumelioti, Z., Kiratzi, A., Melis, N., 2002. Source parameters of the M 6.5 Skyros Island (North Aegean Sea) earthquake of July 26, 2001. Ann. Geophys. 45 (3–4), 513–526.
Benetatos, C., Kiratzi, A., Kementzetzidou, K., Roumelioti, Z., Karakaisis, G., Scordilis, E., Latoussakis, I., Drakatos, G., 2004. The Psachna (Evia Island) earthquake swarm of June 2003. Bull. Geol. Soc. Greece XXXVI (3), 1379–1388.
Chatzipetros, A., Kiratzi, A., Sboras, S., Zouros, N., Pavlides, S., 2013. Active faulting in the north-eastern Aegean Sea Islands. Tectonophysics 597–598, 106–122. http://dx.doi.org/10.1016/j.tecto.2012.11.026 (ISSN 0040-1951).
Chousianitis, K., Ganas, A., Gianniou, M., 2013. Kinematic interpretation of present-day crustal deformation in Central Greece from continuous GPS measurements. J. Geodyn. 71, 1–13.
Chousianitis, K., Ganas, A., Evangelidis, C., 2015. Strain and rotation rate patterns of mainland Greece from continuous GPS data and comparison between seismic and geodetic moment release. J. Geophys. Res. Solid Earth 120. http://dx.doi.org/10.1002/2014JB011762.
Davies, R., England, P., Parsons, B., Billiris, H., Paradissis, D., Veis, G., 1997. Geodetic strain of Greece in the interval 1892–1992. J. Geophys. Res. 102 (B11), 24571–24588. http://dx.doi.org/10.1029/97JB01644.
Font, Y., Kao, H., Lallemand, S., Liu, C.-S., Chiao, L.-Y., 2004. Hypocentral determination offshore Eastern Taiwan using the Maximum Intersection method. Geophys. J. Int. 158, 655–675.
Ganas, A., Papoulia, I., 2000. High-resolution digital mapping of the seismic hazard within the Gulf of Evia rift, Eastern Central Greece using normal fault segments as line sources. Nat. Hazards 22, 203–223.
Ganas, A., Roberts, G., Memou, P., 1998. Segment boundaries, the 1894 ruptures and strain patterns along the Atalanti Fault, Central Greece. J. Geodyn. 26, 461–486.
Ganas, A., Drakatos, G., Pavlides, S.B., Stavrakakis, G.N., Ziazia, M., Sokos, E., Karastathis, V.K., 2005. The 2001 Mw = 6.4 Skyros earthquake, conjugate strike–slip faulting and spatial variation in stress within the central Aegean Sea. J. Geodyn. 39, 61–77.
Ganas, A., Sokos, E., Agalos, A., Leontakianakos, G., Pavlides, S., 2006. Coulomb stress triggering of earthquakes along the Atalanti Fault, Central Greece: two April 1894 M6+ events and stress change patterns. Tectonophysics 420, 357–369.
Ganas, A., Oikonomou, I.A., Tsimi, 2013. NOAfaults: a digital database for active faults in Greece. Bull. Geol. Soc. Greece 47, 518–530.
Ganas, A., Karastathis, V., Moshou, A., Valkaniotis, S., Mouzakiotis, E., Papathanassiou, G., 2014a. Aftershock relocation and frequency–size distribution, stress inversion and seismotectonic setting of the 7 August 2013 M = 5.4 earthquake in Kallidromon Mountain, Central Greece. Tectonophysics 617, 101–113.
Ganas, A., Roumelioti, Z., Karastathis, V., Chousianitis, K., Moshou, A., Mouzakiotis, E., 2014b. The Lemnos 8 January 2013 (Mw = 5.7) earthquake: fault slip, aftershock properties and static stress transfer modeling in the north Aegean Sea. J. Seismol. 18 (3), 433–455. http://dx.doi.org/10.1007/s10950-014-9418-3.
Ghose, S.M., Hamburger, W., Ammon, C.J., 1998. Source parameters of moderate-size earthquakes in the Tien Shan, Central Asia, from regional moment tensor inversion. Geophys. Res. Lett. 25, 3181–3184.
Hatzfeld, D., Ziazia, M., Kementzetzidou, D., Hatzidimitriou, P., Panagiotopoulos, D., Makropoulos, K., Papadimitriou, P., Deschamps, A., 1999. Microseismicity and focal mechanisms at the western termination of the North Anatolian Fault and their implications for continental tectonics. Geophys. J. Int. 137, 891–908.
Husen, S., Hardebeck, J.L., 2010. Earthquake location accuracy. Community Online Resour. Stat. Seism. Anal. http://dx.doi.org/10.5078/corssa-55815573.
Karastathis, V., Ganas, A., Makris, J., Papoulia, J., Dafnis, P., Gerolymatou, E., Drakatos, G., 2007. The application of shallow seismic techniques in the study of active faults: the Atalanti normal fault, Central Greece. J. Appl. Geophys. 62 (3), 215–233.
Karastathis, V., Papoulia, J., Di Fiore, B., Makris, J., Tsambas, A., Stampolidis, A., Papadopoulos, G., 2011. Deep structure investigations of the geothermal field of the North Euboean Gulf, Greece, using 3-D local earthquake tomography and Curie Point Depth analysis. J. Volcanol. Geotherm. Res. 206, 106–120.
Kennett, B.N.L., 1983. Seismic Wave Propagation in Stratified Media. Cambridge University Press, Cambridge.
Kiratzi, A., 2002. Stress tensor inversions along the westernmost North Anatolian Fault Zone and its continuation into the North Aegean Sea. Geophys. J. Int. 151, 360–376.
Konstantinou, K.I., Melis, N., Boukouras, K., 2010. Routine regional moment tensor inversion for earthquakes in the Greek region: the National Observatory of Athens (NOA) database (2001–2006). Seismol. Res. Lett. 81 (5), 750–760.
Koukouvelas, I.K., Aydin, A., 2002. Fault structure and related basins of the North Aegean Sea and its surroundings. Tectonics 21 (5). http://dx.doi.org/10.1029/2001TC901037.
Kranis, H.D., 2007. Neotectonic basin evolution in central-eastern mainland Greece. Bull. Geol. Soc. Greece 40, 360–373.
Kreemer, C., Chamot-Rooke, N., Le Pichon, X., 2004. Constraints on the evolution and vertical coherency of deformation in the Northern Aegean from a comparison of geodetic, geologic and seismologic data. Earth Planet. Sci. Lett. 225, 329–346.
Le Meur, H., 1994. Tomographie Tridimensionnelle a Partir Des Temps Des Premieres Arrivees Des Ondes P et S, Application a la Region de Patras (Grece) (These de Doctorat, Paris VII, France).
Le Meur, H., Virieux, J., Podvin, P., 1997. Seismic tomography of the gulf of Corinth: a comparison of methods. Ann. Geofis. 40 (6), 1–24.
Lomax, A., Curtis, A., 2001. Fast, Probabilistic Earthquake Location in 3D Models Using Oct-Tree Importance Sampling. European Geophysical Society, Nice (March 2001).
Lomax, A., Virieux, J., Volant, P., Berge, C., 2000. Probabilistic Earthquake Location in 3D and Layered Models: Introduction of a Metropolis-Gibbs Method and Comparison with Linear Locations. In: Thurber, C.H., Rabinowitz, N. (Eds.), Advances in Seismic Event Location. Kluwer, Amsterdam, pp. 101–134.

Makropoulos, K., Kaviris, G., Kouskouna, V., 2012. An updated and extended earthquake catalogue for Greece and adjacent areas since 1900. Nat. Hazards Earth Syst. Sci. 12, 1425–1430.

Mettos, A., Rontogianni, T., Papadakis, G., Paschos, P., Georgiou, C., 1991. New data on the geology of the Neogene deposits of the North Euboea. Bull. Geol. Soc. Greece 25 (3), 71–83.

Mettos, A., Rondoyianni, T., Ioakim, C., Papadakis, I., 1992. Evolution geodynamique et reconstruction paloenvironmentale des basins neogenes-quaternaires de la Grece Centrale. Paleontol. Evol. 24-25, 393–402.

Michael, A.J., 1984. Determination of stress from slip data: faults and folds. J. Geophys. Res. 89, 11517–11526.

Moshou, A., Ganas, A., Karastathis, V., Mouzakiotis, E., 2015. Relocation and characteristics of recent earthquake sequences (2013, 2014) on the North Gulf of Evia, Greece. Geophys. Res. Abstr. 17 (EGU2015–14165-1, 2015, EGU General Assembly 2015).

Müller, M.D., Geiger, A., Kahle, H.-G., Veis, G., Billiris, H., Paradissis, D., Felekis, S., 2013. Velocity and deformation fields in the North Aegean domain, Greece, and implications for fault kinematics, derived from GPS data 1993–2009. Tectonophysics 597–598, 34–49. http://dx.doi.org/10.1016/j.tecto.2012.08.003.

Palyvos, N., Bantekas, J., Kranis, H., 2006. Transverse fault zones of subtle geomorphic signature in Northern Evia island (Central Greece extensional province): an introduction to the Quaternary Nileas graben. Geomorphology 76 (3–4), 363–374. http://dx.doi.org/10.1016/j.geomorph.2005.12.002.

Pantosti, D., De Martini, P.M., Papanastassiou, D., Palyvos, N., Lemeille, F., Stavrakakis, G., 2001. A reappraisal of the 1894 Atalanti earthquake surface ruptures, Central Greece. Bull. Seismol. Soc. Am. 91, 760–780.

Papoulia, J., Makris, J., Drakopoulou, V., 2006. Local seismic array observations at north Evoikos, Central Greece, delineate crustal deformation between the North Aegean Trough and Corinthiakos Rift. Tectonophysics 423 (1–4), 97–106.

Pavlides, S.B., Valkaniotis, S., Ganas, A., Keramydas, D., Sboras, S., 2004. The Atalanti active fault: re-evaluation using new geological data. Bull. Geol. Soc. Greece 36, 1560–1567.

Randal, G.E., 1994. Efficient calculation of complete differential seismograms for laterally homogeneous earth models. Geophys. J. Int. 118, 245–254.

Roberts, G.P., Ganas, A., 2000. Fault-slip directions in central and southern Greece measured from striated and corrugated fault planes: comparison with focal mechanism and geodetic data. J. Geophys. Res. B Solid Earth 105 (10), 23,443–223462.

Roberts, S., Jackson, J., 1991. Active Normal Faulting in Central Greece: An Overview. In: Roberts, A.M., Yielding, G., Freeman, B. (Eds.), The Geometry of Normal Faults. Geol. Soc. Sp. Pub. 56, pp. 125–142.

Rondoyanni, T., Galanakis, D., Georgiou, C., Baskoutas, I., 2007. Identifying fault activity in the central Evoikos gulf (Greece). Bull. Geol. Soc. Greece 40, 439–450.

Roumelioti, Z., Kiratzi, A., 2010. Moderate magnitude earthquake sequences in Central Greece (for the year 2008). Bull. Geol. Soc. Greece XLIII, 2144–2153.

Sakellariou, D., Rousakis, G., Kaberi, H., Kapsimalis, V., Georgiou, P., Kanellopoulos, T., Lykousis, V., 2007. Tectono-sedimentary structure and late quaternary evolution of the north Evia gulf basin, Central Greece: preliminary results. Bull. Geol. Soc. Greece XXXVII/1, 451–462.

Stich, D., Ammon, C.J., Morales, J., 2003. Moment tensor solutions for small and moderate earthquakes in the Ibero-Maghreb region. J. Geophys. Res. 108 (B3) (March 2003).

Tarantola, A., Valette, B., 1982. Inverse problems = quest for information. J. Geophys. 50, 159–170.

Vavryčuk, V., 2014. Iterative joint inversion for stress and fault orientations from focal mechanisms. Geophys. J. Int. 199 (1), 69–77. http://dx.doi.org/10.1093/gji/ggu224.

Vernant, P., Reilinger, R., McClusky, S., 2014. Geodetic evidence for low coupling on the Hellenic subduction plate interface. Earth Planet. Sci. Lett. 385 (C), 122–129. http://dx.doi.org/10.1016/j.epsl.2013.10.018.

Walker, R.T., Claisse, S., Telfer, M., Nissen, E., England, P., Bryant, C., Bailey, R., 2010. Preliminary estimate of Holocene slip rate on active normal faults bounding the southern coast of the Gulf of Evia, Central Greece. Geosphere 6 (5), 583–593.